Edinburgh Research Explorer

Properties and phase diagram of (H2S)2H2

Properties and phase diagram of $(H_2S)_2H_2$

Edward J. Pace [ORCID],[1] Xiao-Di Liu [ORCID],[2,*] Philip Dalladay-Simpson,[3] Jack Binns [ORCID],[3,†] Miriam Peña-Alvarez,[1] J. Paul Attfield,[4]
Ross T. Howie,[3] and Eugene Gregoryanz[1,2,3,‡]

[1]*Centre for Science at Extreme Conditions and School of Physics and Astronomy, University of Edinburgh,*
Edinburgh EH9 3FD, United Kingdom
[2]*Key Laboratory of Materials Physics, Institute of Solid State Physics, Chinese Academy of Sciences, Hefei 230031, China*
[3]*Center for High Pressure Science and Technology Advanced Research, Shanghai 201203, China*
[4]*Centre for Science at Extreme Conditions and School of Chemistry, University of Edinburgh, Edinburgh EH9 3FD, United Kingdom*

By combining hydrogen and sulfur within diamond-anvil cells we synthesize $(H_2S)_2H_2$ at 5 GPa and 373 K. Through a series of Raman spectroscopy, infrared spectroscopy, and synchrotron x-ray diffraction experiments we have constrained the phase diagram of $(H_2S)_2H_2$ within a wide *P-T* range. On compression we observe the phase transition sequence of I-II-II′-III, where II′ is a previously unreported phase; at room temperature this sequence spans from 5 to 47 GPa, while the application of low temperatures stabilizes this sequence to 127 GPa (< 80 K). Above these pressures we propose that phase III of $(H_2S)_2H_2$ transforms to a nonmolecular H_3S network. Our Raman and infrared measurements indicate that the transition from $(H_2S)_2H_2$ to H_3S is reversible at room temperature. X-ray diffraction reveals that the symmetry of the underlying S lattice of $(H_2S)_2H_2$ and H_3S is retained along this compression path up to at least 135 GPa.

I. INTRODUCTION

The report of high-temperature superconductivity in dense H_2S has galvanized studies of the high-pressure sulfurhydrogen system [1], yet the composition and nature of bonding in the superconducting phase remain disputed [2–11]. Prior to experimental measurements, two separate theoretical studies predicted abnormally high critical temperatures T_c to emerge from the H_2S ($T_c = 80$ K) [12] and $(H_2S)_2H_2$ ($T_c = 200$ K) [13] systems at very high densities. The latter study predicted a pressure-driven reaction between the molecular H_2 and H_2S components of $(H_2S)_2H_2$ (phase III, *Cccm*) [13]: on compression, the H-H bond softens and then breaks at 111 GPa, reacting with H_2S to form a new phase composed solely of individual H_3S units (*R3m*). At even higher pressure, it was predicted that H_3S would become a nonmolecular, highly symmetrical cubic structure ($Im\bar{3}m$), with a calculated maximum T_c of 204 K at 200 GPa [13,14].

Given the intense interest in the sulfur-hydrogen system, there are surprisingly few direct experiments on $(H_2S)_2H_2$ [6,15–17]. The first experimental observation of superconductivity in this system used pure H_2S as a precursor but claims a maximum T_c of 203 K [1]. However, producing the high-T_c phase required following a convoluted *P-T* path, leading the authors to suggest a decomposition mechanism: $3H_2S \rightarrow 2H_3S + S$. Furthermore, H_2S decomposition models have

found competitive H-S stoichiometries (e.g., H_5S_2) present with H_3S, close to the pressures where the highest T_c is claimed [1,11]. Disproportionated S and other by-products imply that the H_3S product from H_2S is impure, which may account for inconsistent T_c measurements (ranging from 110 to 203 K) reported in experiments using H_2S as a precursor [1,18–21].

Powder x-ray diffraction (XRD) studies of the high-T_c sample detected the disproportionation product S (β-*Po* type) alongside a bcc lattice of S atoms, attributed to $Im\bar{3}m$ H_3S [2]. The pattern can also be better described by S with *Cccm* symmetry [suggested for $(H_2S)_2H_2$], accounting for unidentified "impurity" peaks, which the $Im\bar{3}m$ structure does not do [2,6,22]. Although the volume per S atom of the fitted bcc phase (and also *Cccm*) *does* give an H:S ratio of 3:1, the weak interaction of x rays with hydrogen means there is no information regarding hydrogen atom positions or how S and H are bonded. Indeed, the small distortions between $R3m$ and $Im\bar{3}m$ H_3S structures are indistinguishable under the challenging experimental conditions.

In $(H_2S)_2H_2$ the underlying S-atom configurations are similar across all known experimental and predicted phases, making them difficult to distinguish on the basis of diffraction alone [13,15]. Transitions between high-pressure phases in $(H_2S)_2H_2$ at room temperature are primarily driven by hydrogen bonding (H bonding) and are characterized by the orientation of H_2S molecules and the nature of the H_2 sites within the structure, producing unique vibrational spectra [6,15–17]. In particular the number of H_2 vibrational modes (vibrons) and the effect of compression on their respective frequencies can be utilized to distinguish phase changes and shifts in bond orientation of the surrounding H_2S molecules.

*xiaodi@issp.ac.cn
†Present address: School of Science, RMIT University, Melbourne, Victoria 3000, Australia.
‡e.gregoryanz@ed.ac.uk

Therefore Raman spectroscopy combined with infrared (IR) spectroscopy presents a powerful diagnostic combination for $(H_2S)_2H_2$ at high pressure [15,16], being sensitive to both inter- and intramolecular interactions [23–25].

In this study, we synthesize $(H_2S)_2H_2$ by combining S and H_2 directly in controlled ratios within diamond-anvil cells (DACs). On compression at 300 K, we observe the phase sequence I-II-II'-III, where phase II' is previously unreported. We map out the solid phases of $(H_2S)_2H_2$ from 15 to 300 K, up to 185 GPa. From phase III of $(H_2S)_2H_2$ we observe substantial softening and weakening of the ν_{IIIb} H_2 vibron, with a complete loss of intensity above 50 GPa (300 K) and 127 GPa (80 K); this suggests a reaction between H_2S and H_2 forming an extended sulfur-hydrogen network (H_3S), retaining the initial stoichiometry of 1S:3H but with no H_2 molecules, predicted to occur upon compression of $(H_2S)_2H_2$ [13]. At 300 K we report the reversibility of this transition from both Raman and IR spectroscopy studies. From XRD studies we find that the same S lattice is retained on compression through the H_3S transition, at least up to 135 GPa.

II. EXPERIMENTAL METHODS

DACs with culets of 50–200 μm, containing crystalline sulfur suspended in fluid H_2, were heated to 373 K for 1 h (below 0.5 GPa), then cooled to 300 K, producing discrete fluid domains of H_2S and H_2. Samples were then compressed above 4.8 GPa to form phase I of $(H_2S)_2H_2$ [15,16] in the same manner used to produce $(H_2Se)_2H_2$ [26]. The ratio of H_2:S was controlled by varying the amount of sulfur used, relative to the size of the gasket chamber; we find that $(H_2S)_2H_2$ requires an initial atomic ratio in excess of 3:1 H:S in order to form (equivalent to 3:2 H_2:S). Ratios between 2:1 and 3:1 H:S formed samples of H_2S with excess H_2 but did not tend to transform to $(H_2S)_2H_2$ on further compression, instead behaving in the same manner as pure H_2S. Because of the rich vibrational spectra produced in these experiments we name and number the individual Raman and IR vibrational modes arising from different H_2 environments from $(H_2S)_2H_2$; apart from phase I, all solid phases exhibited two discrete sets of H_2 Raman modes which are herein referred to as *a* (lower frequency) and *b* (higher frequency). Therefore each H_2 vibron ν from $(H_2S)_2H_2$ is denoted by the phase from which it originates (i.e., I, II, II', III), followed by *a* or *b*. For example, the single H_2 vibron from phase I $(H_2S)_2H_2$ is referred to as ν_{Ia}, and phase II exhibits a high-frequency vibron doublet labeled ν_{IIb} and a lower frequency doublet labeled ν_{IIa}; ν_1 refers to *only* pure bulk H_2.

Raman spectroscopy measurements from 17 different samples of $(H_2S)_2H_2$ were collected in a wide temperature range (15–300 K) up to 184 GPa, using 180° backscattering geometry [27]; room temperature experiments were performed with a 514.5-nm Ar$^+$ excitation laser, and low-temperature experiments were performed using a 532-nm solid-state excitation laser, controlling temperature with a modified continuous-flow cryostat using liquid-N_2 (80 K) or liquid-He (< 80 K) cryogens, coupled with two thermostat heaters and proportional-integral-derivative controllers. $(H_2S)_2H_2$ samples were always formed prior to initial cooling. Pressure was calibrated for Raman and IR experiments
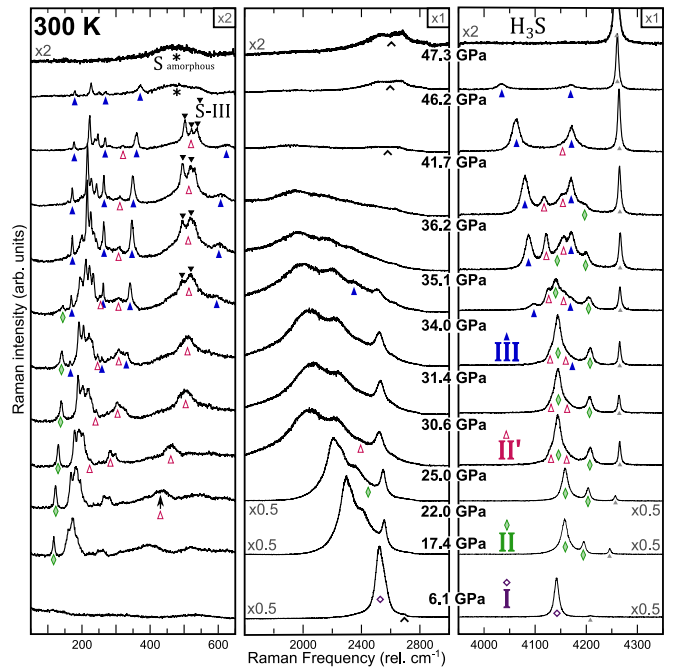

FIG. 1. Raman spectra at increasing pressure for $(H_2S)_2H_2$ at 300 K. Key excitations are highlighted for phase II (green diamonds), phase II' (magenta open triangles), and phase III (blue solid triangles). Small gray triangles indicate H_2-ν_1. Excitations corresponding to crystalline sulfur (downward triangles), amorphous sulfur (asterisks), and second-order diamond (carats) are also indicated. Relative scales of each panel are indicated in the top right; scaling of individual spectra is labeled where applicable.

with a combination of ruby fluorescence [28,29] and Raman shift of the diamond edge [30]. The mid-IR spectra were collected in transmission mode with a Bruker Vertex 80v Fourier transform IR spectrometer and a Hyperion 2000 IR microscope equipped with a nitrogen-cooled mercury cadmium telluride detector. Synchrotron XRD data were collected up to 135 GPa (300 K) from four separate runs. Angle dispersive XRD measurements were recorded at room temperature at the following beamlines and synchrotrons (wavelengths): P2.02 at PETRA III (Germany; 0.2922 Å), GSECARS at Advanced Photon Source (United States; 0.3344 Å), and I-15 at the Diamond Light Source (United Kingdom; 0.4246 Å). XRD experiments utilized a combination of ruby fluorescence, the Raman diamond edge, and Au pressure markers, calibrated using the Vinet equation of state [31].

III. RESULTS

Phase I was identified upon compression of H_2S and H_2 between 4.7 and 5.3 GPa (300 K) from a single additional H_2 Raman vibron at 4140 cm^{-1} (ν_{Ia}), redshifted relative to H_2 ν_1 [Figs. 1, 2(a), and 3]. An IR absorption attributed to the guest H-H stretch was also observed at a frequency very close to the ν_{Ia} Raman mode [Figs. 2(a) and 3]. A Rietveld refinement of diffraction data collected at 6.1 GPa confirmed the tetragonal $I4/mcm$ structure [$a = 7.183(1)$, $c = 5.902(1)$ Å], in agreement with a previous study [15,22].
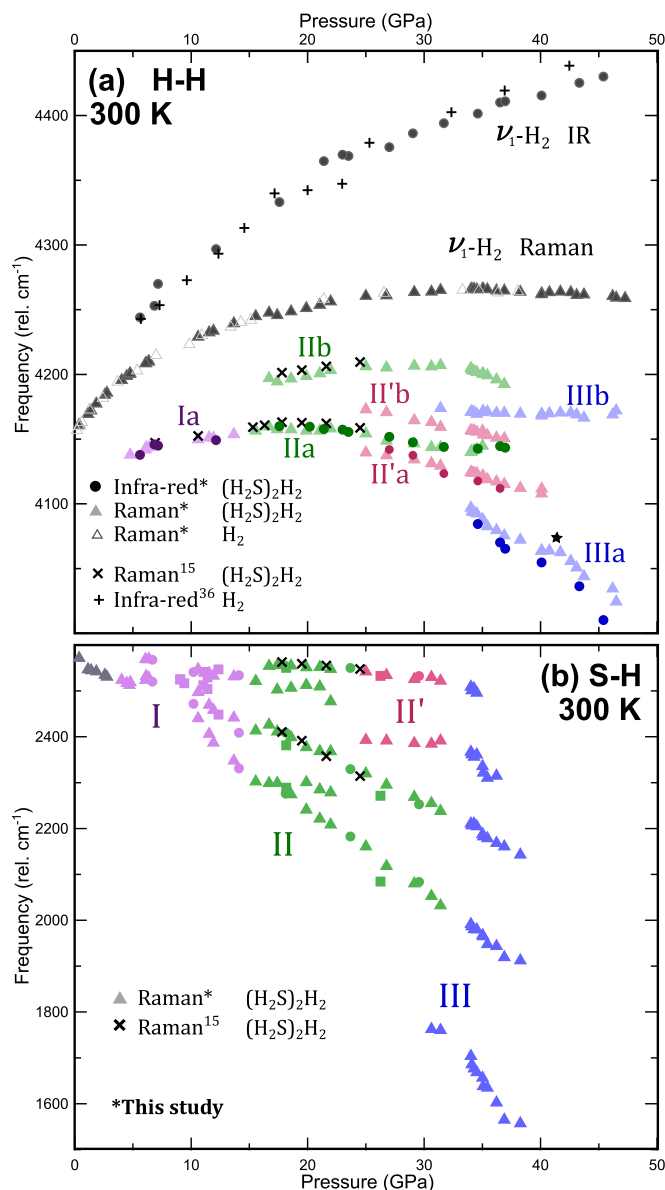
FIG. 2. (a) Raman frequencies (relative cm^{-1}; solid triangles) and infrared absorption frequencies (cm^{-1}; darker circles) for H$_2$ vibrons from (H$_2$S)$_2$H$_2$, plotted as a function of pressure (GPa) at 300 K, showing transitions between phases I (purple), II (green), II$'$ (magenta), and III (blue). Free molecular H$_2$ vibron frequencies from the (H$_2$S)$_2$H$_2$ samples (solid gray triangles) are shown alongside data from pure H$_2$ (open gray triangles). Data replotted from other studies are represented by cross symbols for (H$_2$S)$_2$H$_2$ (Raman) [15] and plus symbols for pure H$_2$ (IR) [32]. (b) Raman frequencies (relative cm^{-1}) for S-H stretching modes from (H$_2$S)$_2$H$_2$, plotted as a function of pressure (GPa) at 300 K. Different symbols refer to different experimental runs, while cross symbols are replotted from a previous study [15].

Phase II can be reached on cooling below 173 K (10 GPa) or on compression above 16.7 GPa at room temperature, resulting in a negative slope between the I-II transition pressure at room temperature and lower temperatures (Fig. 4). Phase II is identified by the characteristic splitting of the S-H Raman vibrational stretching mode ($\sim$2400 cm^{-1}) and

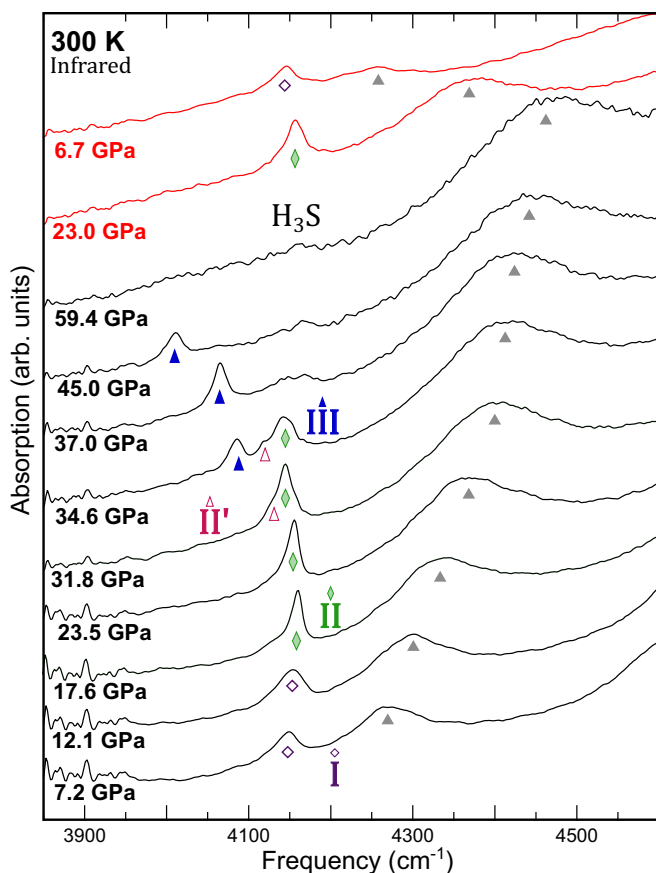FIG. 3. IR absorption spectra of H-H stretches from (H$_2$S)$_2$H$_2$, plotted as a function of increasing pressure (black) and decreasing pressure (red; GPa). Phases are labeled with the same colors and symbols as in previous figures.

splitting of ν_{Ia} into ν_{IIa} and ν_{IIb} [Figs. 1, 2(a), 5, and 6]. No change was observed in atomic volume by diffraction at room temperature, in agreement with a previous study [15]. Phase II is easily recognized by the emergence of lattice modes (Figs. 1 and 5) arising from the orientational ordering of H$_2$S molecules; the strengthening of H bonding between neighboring H$_2$S molecules restricts their free rotation, which also breaks the degeneracy of the symmetric and asymmetric S-H stretches. A comparable effect is observed in Raman studies on compression of pure H$_2$S (and D$_2$S) from phase I-I$'$-IV [33–35]. We also observe a large increase in the IR absorption of the S-H stretching mode ($\sim$2300 cm^{-1}) at the phase transition (I-II), reflecting the change in dipole moment of the S-H bonds [22]. For (H$_2$S)$_2$H$_2$, at room temperature we observe two H$_2$ Raman vibrons (ν_{IIa} and ν_{IIb}) and four broad S-H stretching modes (between 2200 and 2600 cm^{-1}; Fig. 1); [15,16] at low temperatures we find at least seven narrow S-H stretching modes ($\sim$2250-2580 cm^{-1}) and observe two doublets of H-H Raman vibrons (ν_{IIa} and ν_{IIb}, Figs. 5 and 6). On compression of phase II at room temperatures and below, the S-H stretching modes rapidly broaden and decrease in frequency [Fig. 2(b)], indicating a significant enhancement of the H-bond strength between neighboring H$_2$S molecules. From IR spectroscopy, we observe a reduction in the FWHM of the H-H IR vibron at the transition pressure from phase I to
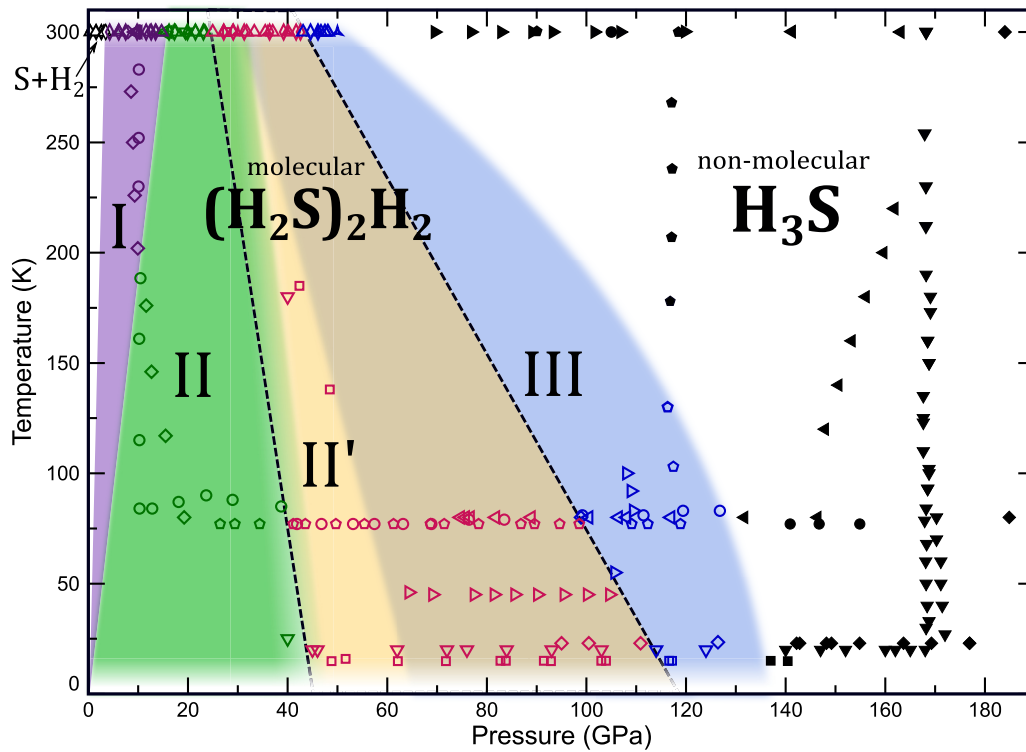
FIG. 4. Proposed phase diagram for the solid phases of $(H_2S)_2H_2$. Symbols represent different experimental runs, while their colors represent different phases: purple, I; green, II; magenta, II′; blue, III; and black, H_3S. The dotted line outlines a translucent yellow area indicating the stability field of II′: The overlapping colors from phases II and III within this stability field indicate the phase overlap. The white region indicates where nonmolecular H_3S is stable.

phase II (Fig. 3), while its frequency retains the same pressure dependence of ν_{IIa}. This reduction in IR bandwidth, coupled with the positive slope of the $\nu_{IIa/b}$ Raman mode frequencies, reflects a reduced interaction between H_2 and H_2S within phase II of the compound; this is due to an enhanced interaction between the H_2S molecules themselves upon orientational ordering, as H bonding strengthens until it overcomes the energy of rotation, which then induces the lattice modes.

Above 25 GPa (300 K) and 39 GPa (> 80 K) we observe new lattice modes and previously unidentified H-H Raman vibrons ($\nu_{II'a}$ and $\nu_{II'b}$, magenta open triangles in Fig. 1), which we attribute to a previously unreported $(H_2S)_2H_2$ phase, II′, which coexists with phases II and III. The H:S stoichiometry of II′ is assumed to remain 3:1, as no change was observed in the atomic volume at the transition (Fig. 7). It should be noted that at 300 K only two II′ vibrons are visible [Figs. 1 and 2(a)], but $\nu_{II'b}$ exhibits a high-frequency shoulder below 80 K (Figs. 5 and 6). IR measurements detect only one vibron with a frequency very close to $\nu_{II'a}$. Phase II′ also exhibits the following distinct Raman characteristics at 300 K: development of a librational mode (460 cm^{-1} at 25 GPa, 300 K indicated on Fig. 1); an abrupt drop in frequency in one S-H stretching mode (highlighted in the middle panel of Fig. 1), with a change in pressure dependence [Fig. 2(b)]; and a further increase in the bandwidth and marked decrease in overall intensity for all S-H stretching modes (Fig. 1; note scaling of first two spectra in middle panel). Increasing pressure above 25 GPa (300 K) sees the continued broadening of the S-H stretches.

We observe Raman vibrons ν_{IIIa} and ν_{IIIb} from 34.0 GPa (300 K), with one IR active vibron with a frequency similar to ν_{IIIa}. The corresponding phase III lattice modes appeared from 31.4 GPa at 300 K (Fig. 1) and 53 GPa below 80 K (Fig. 5). At 300 K the phase overlap after the II′ to III transition was around 10 GPa: this phase overlap increases at lower temperatures such that phase II′ is stable up to 42 GPa at 300 K, 99 GPa at 80 K, 105 GPa at 45 K, and 112 GPa at 25 K (Fig. 4), which we use to map a straight phase boundary with a slope of approximately −4 K GPa^{-1} (rightmost dotted line Fig. 4).

Figure 2(b) shows a marked increase in the slopes of three S-H stretching modes (around 1775, 2375, and 2500 cm^{-1}, at 34 GPa), around the phase II-III transition pressure. This indicates that the intermolecular interactions are greater in phase III of $(H_2S)_2H_2$ and that the S-H bonds are longer and weaker than in the previous phases. This could be interpreted as the H bonds approaching symmetrization in phase III, whereby the H atom becomes equidistant between the two S atoms [17]. A similar shift in the pressure dependence of the ν_{IIIa} Raman mode and the sole IR mode is shown in Fig. 2(a) (marked with a star). On further compression, the frequency of ν_{IIIa} steadily decreases with a gradual reduction in intensity, up to a maximum pressure of 46 GPa (300 K) and 127 GPa (80 K), above which it was no longer observed. The IR mode exhibits the same behavior (Fig. 3), and the lattice modes also disappear around the same pressures (Figs. 1 and 5). We interpret these observations as a transition from $(H_2S)_2H_2$ to an extended sulfur-hydrogen network following the loss
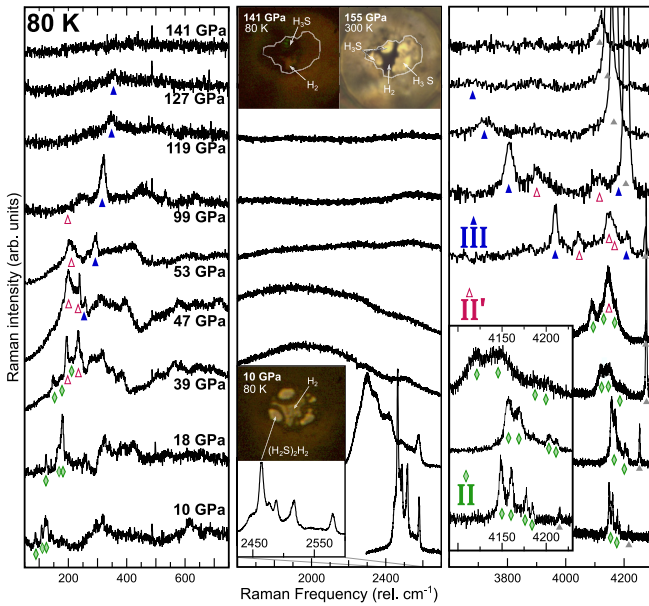
FIG. 5. Raman spectra at increasing pressures for $(H_2S)_2H_2$ at 80 K. Key excitations are highlighted for phase II (green diamonds), phase II′ (magenta open triangles), and phase III (blue solid triangles). Small gray triangles indicate H_2-ν_1. Insets show photomicrographs of the sample at the indicated conditions.

FIG. 6. Raman frequencies (relative cm^{-1}) for H_2 vibrons from $(H_2S)_2H_2$, plotted as a function of pressure (GPa) at different temperatures. Symbols refer to the temperatures indicated in the inset, and the data points are plotted in Fig. 4. The stable pressure ranges for each solid phase at 80 K are represented by the bordered boxes at the bottom; solid boxes with stable ranges at 300 K are shown above for reference.

of molecular integrity from the H-H bond breaking and symmetrization from H-bonding between the H_2S molecules [13]. We observe no evidence that the stoichiometric ratio of H:S changes from 3:1; therefore we refer to the sulfur-hydrogen network as H_3S. Indeed, the change in the ν_{IIIa} and ν_{IIIb} stretching mode frequencies aligns well with previous theoretical calculations for the internal H-H bond lengths within the *Cccm* structure (phase III) [13]. In addition, at 300 K we find the transition to a nonmolecular network to be reversible, with the Raman and IR signatures of $(H_2S)_2H_2$ returning on decompression (Figs. 3 and 8).

In contrast to the rich Raman and IR spectra arising from the reorientation of H_2S and rearrangement of H_2 molecules, diffraction studies show almost no changes to the underlying sulfur lattice throughout the solid phases of $(H_2S)_2H_2$, and H_3S. Figure 7 shows a plot of atomic volume per S atom as a function of pressure; we observe no sudden volume decreases at any of the transition pressures observed in our Raman and infrared experiments. This indicates that the stoichiometry remains 3H:1S. The inset plot of diffraction peaks vs pressure shows no obvious splitting or merging of peaks throughout the solid phases of $(H_2S)_2H_2$ and above the H_3S transition, which suggests that H_3S forming directly from compression of $(H_2S)_2H_2$ (at 300 K) maintains the same underlying S sublattice observed throughout all phases of $(H_2S)_2H_2$; the space group symmetry is congruous with that of a tetragonal $I4/mcm$ lattice [15] or an orthorhombic *Cccm* lattice at least up to 50 GPa [6,13]. A sample recovered from 80 to 300 K (at 146 GPa) was fitted with *Cccm* symmetry, giving statistically significant splitting of the (131/311) peak positions (Fig. 9) and was visually highly reflective, as shown in the inset in Fig. 5.
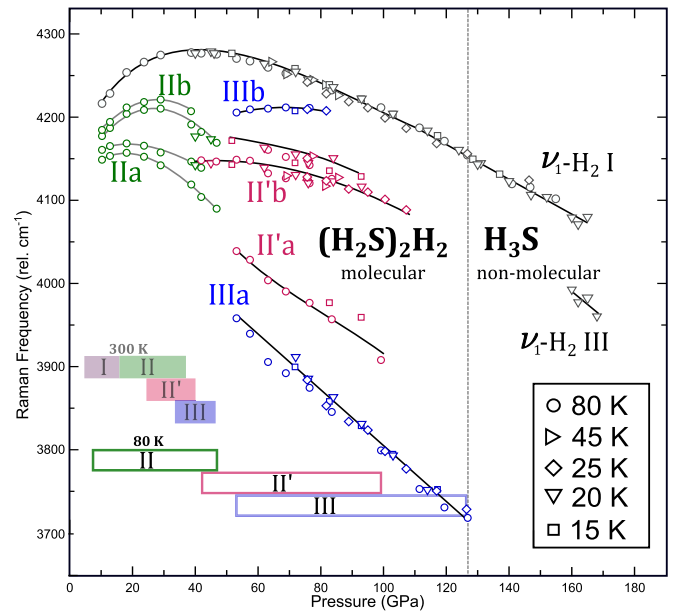
IV. DISCUSSION AND CONCLUSIONS

Figure 4 shows our proposed phase diagram of $(H_2S)_2H_2$ based on our Raman and IR data points. The significant phase overlap of phases II and III with II′ is represented by the stability field of II′, surrounded by dotted black lines. The white region indicates the proposed stability field of the H_3S phase, where no vibrational modes from H_2 molecules are observed by either Raman or IR spectroscopy. The phase diagram highlights the significant enhancement of the stable pressure ranges at low temperatures; most notably, the difference in the H_3S transition pressure moves from 47 GPa at 300 K to 127 GPa at 80 K. The expansion of the respective stability fields of the $(H_2S)_2H_2$ phases at low temperatures also reflects the overall stability of the compound with respect to decomposition at high pressures.

In some room temperature studies we observe partial decomposition from laser overexposure in samples of $(H_2S)_2H_2$ and H_3S (and pure H_2S). This is evidenced by a broad Raman excitation at 475 relative cm^{-1} (Fig. 1), which we attribute to the formation of an S-S bond within amorphous sulfur, from degradation of the H_2S molecules. Previous Raman studies have also reported a broad peak at the same frequency, attributed to the formation of S-S bonds on compression of D_2S [36–38]. We find that laser-induced decomposition is more sensitive at higher pressures and was observed only at room temperature. Throughout the phase sequence I-II-II′-III, $(H_2S)_2H_2$ progressively loses molecular integrity of both H_2S and the H_2 ν_a environments, which could explain the increased sensitivity at higher pressures with respect to decomposition (at 300 K). This sensitivity appears restricted to
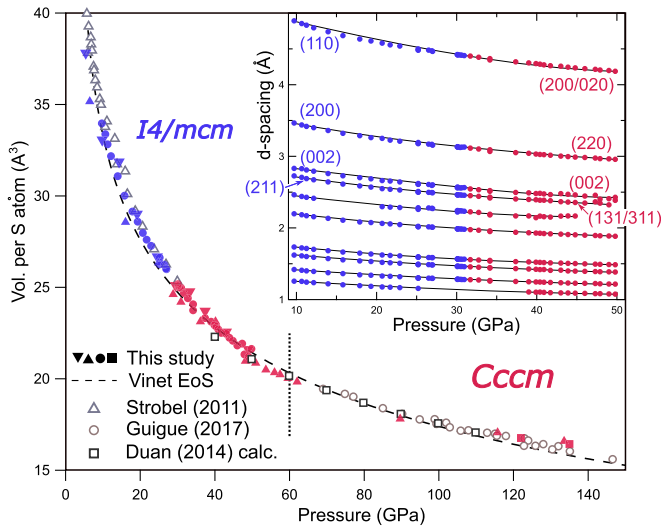
FIG. 7. Vinet equation of state based on the sulfur atomic volume in $(H_2S)_2H_2$ and H_3S up to 150 GPa. $V_0 = 39.26$ Å^3, $K_0 = 16.7(5)$ GPa, $K' = 5.39(8)$. V_0 is set at 4.8 GPa, where $(H_2S)_2H_2$ forms. Blue points are calculated volumes from refinements of $I4/mcm$ symmetry, and maroon points are calculated volumes from refinements of the $Cccm$ structure. Gray open triangles are plotted from Ref. [15], gray open circles are plotted from Ref. [6], and black open squares are calculated volumes from Ref. [13]. The inset shows a plot of d spacings as a function of pressure up to 50 GPa; we observe no splitting of the (131/311) peak in $Cccm$ up to 50 GPa. The same volumes could hence be obtained from either $I4/mcm$ or $Cccm$.

wavelengths around the visible spectrum, as S was observed in only one diffraction study where the sample was also probed with a Raman laser. We previously reported sensitivity to laser-induced decomposition in the electronically analogous $(H_2Se)_2H_2$ [26]. By maintaining low laser powers in our $(H_2S)_2H_2$ experiments we were able to avoid sample degradation and demonstrate the reversibility of the H_3S transition with both Raman (Fig. 8) and IR measurements (Fig. 3). In a prior study of $(H_2Se)_2H_2$, decomposition of the compound above the metallization pressure of Se was misinterpreted as metallization of H_3Se [39,40].

Although we were able to synthesize single crystals of H_2S from S and H_2, upon formation of $(H_2S)_2H_2$ the sample tended to break up into a small number of crystallites, resulting in poor powder diffraction patterns, an issue that was also raised in a previous study of $(H_2S)_2H_2$ [15]. As such, experimental determination of the structures of $(H_2S)_2H_2$ by XRD is inherently limited. Currently, the proposed structures for $(H_2S)_2H_2$ come from theoretical calculations: the suggested space group symmetries are $I4/mcm$ [15] (phase I), $I222$ [15] or $P1$ [13] (phase II), and $Cccm$ [13] (phase III). It is worth noting here that the $I4/mcm$ (tetragonal) and $Cccm$ (Orthorhombic) symmetries are indistinguishable if the unit cell dimensions a and b for $Cccm$ are equal within experimental uncertainties. From factor group analysis we can rule out space group $P1$, proposed as the only stable structure below 40 GPa [13]; $P1$ allows only three possible IR/Raman lattice modes, which is not congruent with the experimental data (Figs. 1, 3, and 5). Such analysis does not rule out any of the other space groups which allow a sub-
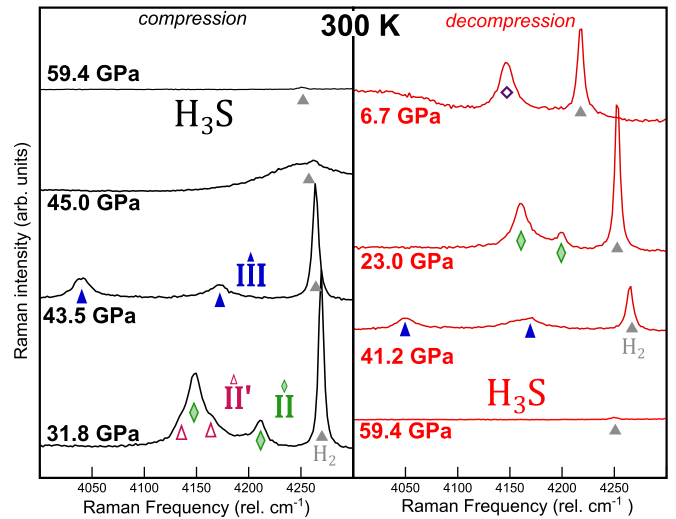

FIG. 8. Raman spectra for $(H_2S)_2H_2$ and H_3S as a function of increasing pressure (black) and decreasing pressure (red) at 300 K, demonstrating the reversibility of the $(H_2S)_2H_2$ to H_3S transition. Low laser powers prevented amorphization of sulfur and decomposition of sulfur hydrides.

stantially greater number of lattice modes than are observed. It is also unlikely that $I222$ is responsible for phase II, as the structure predicts only two H_2 environments, while our low-temperature data reveal there are indeed four (two pairs) of H_2 environments in phase II (Fig. 5).

From XRD we can detect only the relative positions of the S atoms, and therefore the primary evidence for $Cccm$ in phase III or H_3S from diffraction would be if the (131/311) peak split; this would signify that the unit cell dimension a was no longer equal to b, as it is for the tetragonal $I4/mcm$ symmetry. We do not clearly observe any peaks visibly splitting in our diffraction data (or in data from other studies of H_3S [6,17]), yet the differences between our refined values of a and b are statistically significant (Fig. 9). Despite the fact that competitive H_3S structures have been reported in the relevant pressure ranges (e.g., $C2/c$ [11]), $Cccm$ still presents the best stable structural candidate for phase III, which agrees with the experimental Raman data [13,41]; $Cccm$ has two H_2 environments compared to the single environment of $I4/mcm$ [15], and the predicted H-H bond lengths as a function of pressure for $Cccm$ also correspond very well to the observed frequency dependences of $\nu_{IIIa/b}$ [13] [Figs. 1, 2(a), 5, and 6]. Although none of the structures can be claimed to be explicitly true, $Cccm$ remains the best approximation of the phase III structure from an assessment of all existing studies.

Given that the transition from $(H_2S)_2H_2$ to H_3S appears to result from a gradual lengthening of the internal chemical bonds of H_2S and H_2, the H_3S structure is likely to be very similar to phase III of $(H_2S)_2H_2$ but with slightly shifted H atomic positions. At the very least, our diffraction data can discern the difference between orthorhombic-based ($Cccm$ or equivalent) and a more symmetrical bcc cubic S lattice (i.e., $Im\bar{3}m$ or $R3m$). Although the orthorhombic-based and cubic-based symmetries have common peaks, the bcc pattern produces far fewer reflections. Previously, both $Cccm$ [6] and $Im\bar{3}m$ [17] structures were reported as stable crystalline
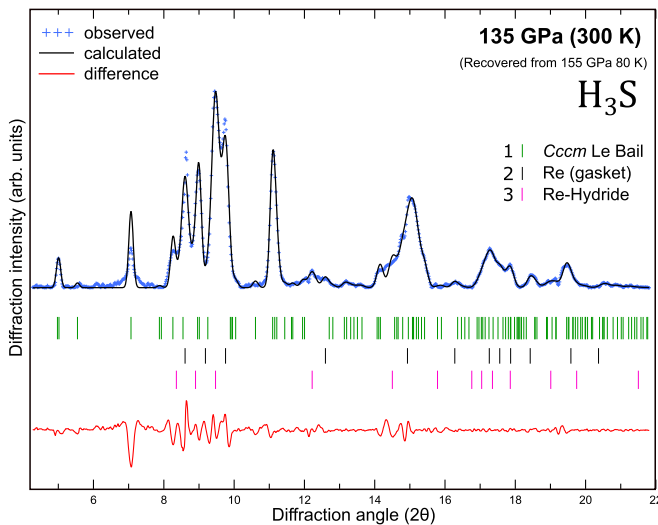
FIG. 9. Integrated diffraction data of H_3S at 135 GPa, obtained from the $(H_2S)_2H_2$ sample compressed at low temperature (giving the data shown in Fig. 5) and recovered to 300 K. The data are fitted with a Le Bail refinement of $Cccm$ symmetry [$a = 7.645(2)$ Å, $b = 7.697(2)$ Å, and $c = 4.481(1)$, $\chi^2 = 4.04$]; $\lambda = 0.3344$ Å.

phases after laser heating S in H_2. Similarly, the first structural study of the high-T_c phase (from decomposition of H_2S) claims the pattern is bcc S but has impurity peaks which match the orthorhombic-based structure, alongside the additional reflections from the excess by-product of pure S [2]; at the least, it cannot be said to be purely bcc S. Recently, it was shown that subsequent laser heating of the poorly crystallized mixture produces a much cleaner bcc S phase, without any of the orthorhombic peaks and only minor impurities [42]. Theoretical calculations find a high kinetic barrier between the phase with an orthorhombic-based S lattice and a cubic-based S lattice [13]. Given both structures are reported from laser-heating experiments where H_3S is produced from S and H_2 [6,17] and laser heating of H_3S (produced from H_2 decomposition) seems to favor the formation of the cubic phase, we can posit that the orthorhombic-based structure is generally more stable than the cubic-based structure. We speculate that the pure orthorhombic-based H_3S, produced from compression of $(H_2S)_2H_2$, would become the high-T_c cubic phase if heated. A wide range of T_c values is reported across multiple studies of the high-T_c phase where H_2S is used as a precursor, and the samples are only "annealed" at room temperature [1,18–21]; it is possible that the pressure-induced decomposition of H_2S produces a mixture of orthorhombic, cubic, and pure S phases.

While it remains experimentally unfeasible to determine the atomic positions of hydrogen in $(H_2S)_2H_2$ and H_3S phases, our spectroscopic data offer substantial insight into their behavior. An important question is raised by the observation that the detected IR absorption frequencies of the H-H stretch in $(H_2S)_2H_2$ are nearly identical to the Raman excitation frequencies of H_2 ν_a vibrons as functions of pressure, from all of the solid phases, I-II-II′-III (Fig. 3); the IR frequencies even match subtle shifts in pressure dependence, for example, in ν_{IIIa} [indicated by a star in Fig. 2(a)], as well as mirroring a slight increase in frequency of ν_{IIa} around 30 GPa [Fig. 2(a)]. It is reasonable to assume that this is not coincidental and that the IR absorptions also occur from the same ν_a vibrational modes. Because the selection rules for $I4/mcm$ and $Cccm$ forbid the same IR and Raman lattice vibrational modes, it could be interpreted that the H_2 ν_b molecules are aligned such that their vibration becomes coupled to the lattice phonons of the compound and hence are only observed by Raman spectroscopy and not in the IR spectra. This in turn would imply the internal vibrations of H_2 ν_a molecules remain uncoupled to the lattice vibrations, possibly due to rotation, and hence the symmetry based selection rules do not apply. The lower frequency of ν_a indicates these H_2 molecules experience more local interaction with the H_2S molecules themselves. Perhaps this is due to a greater dipole moment on each H_2S, as the H bonding becomes enhanced at higher pressures, which in turn contributes to the weakening of the ν_{IIIa} Raman mode at higher pressures, facilitating the subsequent transformation to an extended sulfur-hydrogen H_3S network. These results provide a benchmark for future studies of the sulfur-hydrogen system. The enhanced stability of $(H_2S)_2H_2$ and H_3S at low temperatures and the retention of the S lattice structure contribute to understanding the mechanisms by which other sulfur-hydride phases are adopted at high pressures.

[1] A. P. Drozdov, M. I. Eremets, I. A. Troyan, V. Ksenofontov, and S. I. Shylin, Nature (London) **525**, 73 (2015).

[2] M. Einaga, M. Sakata, T. Ishikawa, K. Shimizu, M. I. Eremets, A. P. Drozdov, I. A. Troyan, N. Hirao, and Y. Ohishi, Nat. Phys. **12**, 835 (2016).

[3] R. Akashi, W. Sano, R. Arita, and S. Tsuneyuki, Phys. Rev. Lett. **117**, 075503 (2016).

[4] E. E. Gordon, K. Xu, H. Xiang, A. Bussmann-Holder, R. K. Kremer, A. Simon, J. Köhler, and M. H. Whangbo, Angew. Chem. Int. **55**, 3682 (2016).

[5] A. F. Goncharov, S. S. Lobanov, I. Kruglov, X.-M. Zhao, X.-J. Chen, A. R. Oganov, Z. Konôpková, and V. B. Prakapenka, Phys. Rev. B **93**, 174105 (2016).

[6] B. Guigue, A. Marizy, and P. Loubeyre, Phys. Rev. B **95**, 020104(R) (2017).

[7] I. Kruglov, R. Akashi, S. Yoshikawa, A. R. Oganov, and M. M. D. Esfahani, Phys. Rev. B **96**, 220101(R) (2017).

[8] R. Szczęśniak and A. P. Durajski, Sci. Rep. **8**, 6037 (2018).

[9] M. Kostrzewa, R. Szczęśniak, J. K. Kalaga, and I. A. Wrona, Sci. Rep. **8**, 11957 (2018).

[10] A. Majumdar, J. S. Tse, and Y. Yao, Sci. Rep. **9**, 5023 (2019).

[11] T. T. Cui, D. Chen, J. C. Li, W. Gao, and Q. Jiang, New J. Phys. **21**, 033023 (2019).

[12] Y. Li, J. Hao, H. Liu, Y. Li, and Y. Ma, J. Chem. Phys. **140**, 174712 (2014).

[13] D. Duan, Y. Liu, F. Tian, D. Li, X. Huang, Z. Zhao, H. Yu, B. Liu, W. Tian, and T. Cui, Sci. Rep. **4**, 6968 (2014).

[14] I. Errea, M. Calandra, C. J. Pickard, J. R. Nelson, R. J. Needs, Y. Li, H. Liu, Y. Zhang, Y. Ma, and F. Mauri, Nature (London) **532**, 81 (2016).

[15] T. A. Strobel, P. Ganesh, M. Somayazulu, P. R. C. Kent, and R. J. Hemley, Phys. Rev. Lett. **107**, 255503 (2011).

[16] S. Duwal and C.-S. Yoo, J. Phys. Chem. C **121**, 12863 (2017).

[17] A. F. Goncharov, S. S. Lobanov, V. B. Prakapenka, and E. Greenberg, Phys. Rev. B **95**, 140101(R) (2017).

[18] A. P. Drozdov, M. I. Eremets, and I. A. Troyan, arXiv:1412.0460.

[19] I. Troyan, A. Gavriliuk, R. Rüffer, A. Chumakov, A. Mironovich, I. Lyubutin, D. Perekalin, A. P. Drozdov, and M. I. Eremets, Science **351**, 1303 (2016).

[20] F. Capitani, B. Langerome, J. B. Brubach, P. Roy, A. Drozdov, M. I. Eremets, E. J. Nicol, J. P. Carbotte, and T. Timusk, Nat. Phys. **13**, 859 (2017).

[21] S. Mozaffari, D. Sun, V. S. Minkov, A. P. Drozdov, D. Knyazev, J. B. Betts, M. Einaga, K. Shimizu, M. I. Eremets, L. Balicas, and F. F. Balakirev, Nat. Commun. **10**, 2522 (2019).

[22] See Supplemental Material at http://link.aps.org/supplemental/10.1103/PhysRevB.xx.xxxxxx for additional Raman spectra, IR spectra, and diffraction data.

[23] J. Binns, X.-D. Liu, P. Dalladay-Simpson, V. Afonina, E. Gregoryanz, and R. T. Howie, Phys. Rev. B **96**, 144105 (2017).

[24] J. Binns, P. Dalladay-Simpson, M. Wang, G. J. Ackland, E. Gregoryanz, and R. T. Howie, Phys. Rev. B **97**, 024111 (2018).

[25] R. Turnbull, M. E. Donnelly, M. Wang, M. Peña-Alvarez, C. Ji, P. Dalladay-Simpson, H. K. Mao, E. Gregoryanz, and R. T. Howie, Phys. Rev. Lett. **121**, 195702 (2018).

[26] E. J. Pace, J. Binns, M. Peña Alvarez, P. Dalladay-Simpson, E. Gregoryanz, and R. T. Howie, J. Chem. Phys. **147**, 184303 (2017).

[27] A. F. Goncharov, Int. J. Spectrosc. **2012**, 16 (2012).

[28] H. K. Mao, J. Xu, and P. M. Bell, J. Geophy. Res. **91**, 4673 (1986).

[29] A. Dewaele, M. Torrent, P. Loubeyre, and M. Mezouar, Phys. Rev. B **78**, 104102 (2008).

[30] Y. Akahama and H. Kawamura, J. Phys.: Conf. Ser. **215**, 012195 (2010).

[31] A. Dewaele, P. Loubeyre, and M. Mezouar, Phys. Rev. B **70**, 094112 (2004).

[32] M. Hanfland, R. J. Hemley, H. K. Mao, and G. P. Williams, Phys. Rev. Lett. **69**, 1129 (1992).

[33] H. Shimizu, H. Yamaguchi, S. Sasaki, A. Honda, S. Endo, and M. Kobayashi, Phys. Rev. B **51**, 9391(R) (1995).

[34] S. Sasaki and H. Shimizu, J. Phys. Soc. Jpn. **64**, 3309 (1995).

[35] J. S. Loveday, R. J. Nelmes, S. Klotz, J. M. Besson, and G. Hamel, Phys. Rev. Lett. **85**, 1024 (2000).

[36] M. Sakashita, H. Yamawaki, H. Fujihisa, K. Aoki, S. Sasaki, and H. Shimizu, Phys. Rev. Lett. **79**, 1082 (1997).

[37] M. Sakashita, H. Fujihisa, Yamawaki, and K. Aoki, J. Phys. Chem. A **104**, 8838 (2000).

[38] S. Duwal and C.-S. Yoo, J. Phys. Chem. C **120**, 21770 (2016).

[39] X. Zhang, W. Xu, Y. Wang, S. Jiang, F. A. Gorelli, E. Greenberg, V. B. Prakapenka, and A. F. Goncharov, Phys. Rev. B **97**, 064107 (2018).

[40] E. J. Pace, J. Binns, P. Dalladay-Simpson, R. T. Howie, and M. Peña Alvarez, Phys. Rev. B **98**, 106101 (2018).

[41] J. A. Flores-Livas, A. Sanna, and E. K. U. Gross, Eur. Phys. J. B **89**, 63 (2015).

[42] H. Nakao, M. Einaga, M. Sakata, M. Kitagaki, K. Shimizu, S. Kawaguchi, N. Hirao, and Y. Ohishi, J. Phys. Soc. Jpn. **88**, 123701 (2019).